Nonreciprocal Entanglement of Frequency-Distinct Qubits

Sajjad Taravati

Faculty of Engineering and Physical Sciences, University of Southampton, Southampton SO17 1BJ, UK
Email Address: s.taravati@soton.ac.uk

Keywords: *Superconducting quantum devices, Metasurfaces, Quantum entanglement, Space-Time*

Entanglement is the linchpin of quantum mechanics and a pivotal enabler of quantum technologies, wherein the states of particles are intrinsically correlated, such that the state of one instantaneously influences the other, regardless of the distance between them. Reciprocal entanglement and coupling between qubits often lead to unwanted bidirectional interactions and reflections, which degrade quantum states and reduce quantum coherence. This paper introduces a cryogenic-compatible metasurface that leverages space-time modulation to enable nonreciprocal entanglement between frequency-distinct superconducting qubits. This functionality is achieved through a reflective quantum state-converting metasurface, specifically designed for millikelvin-temperature quantum technologies. The metasurface utilizes cascaded space-time-modulated Josephson field-effect transistors (JoFETs), offering a transformative platform for advanced quantum state manipulation and entanglement. This spatiotemporal superconductor-semiconductor metasurface transcends the limitations of traditional linear space-time metasurfaces by incorporating gate-controlled Josephson junctions, offering highly efficient spurious-free state-frequency conversion. This study demonstrates that spatiotemporal superconducting metasurfaces, particularly those leveraging JoFETs, enable highly efficient quantum state conversion even for superconducting qubits with a high frequency distinction ratio.

1 Introduction

Quantum entanglement is the foundation of quantum mechanics, representing bidirectional interactions between particles operating at identical frequencies, where each particle influences the other's state and becomes correlated through quantum operations or entangling gates [1, 2, 3, 4]. In these cases, the measurement of one qubit instantaneously affects the state of the other, irrespective of how far apart they are or what lies between them, maintaining symmetry in the quantum interaction. However, creating this fundamental phenomenon becomes significantly more challenging when qubits operate at different energy levels (frequencies) or when unidirectional entanglement is required [5]. Frequency conversion is crucial for advancing quantum technologies, enabling the transfer and manipulation of quantum information across different frequency bands [6, 5, 7, 8, 9, 10]. This is essential for integrating quantum nodes with disparate frequencies, such as superconducting qubits, trapped ions, and optical photons, in hybrid quantum networks. Superconducting frequency converters are particularly valuable due to their ultra-low loss and high coherence, which preserve quantum states and ensure minimal information degradation. In quantum computing, frequency converters can manage qubit interactions and reduce crosstalk, crucial for maintaining qubit fidelity and implementing error correction [11, 12]. In addition, they can transfer quantum states from microwave photons to optical photons, which are ideal for long-distance communication and accessing long-lived quantum memories, thus expanding quantum computing networks and enhancing hybrid quantum systems [8]. In quantum sensing, their ability to operate at millikelvin temperatures with minimal noise enhances sensitivity and precision, making them ideal for applications like dark matter detection [13, 14, 15].

Parametric interactions in superconducting circuits, such as those in Josephson parametric amplifiers (JPAs) and traveling-wave parametric amplifiers (JTWPAs), have been widely studied for phase-sensitive amplification and frequency conversion [16, 17, 18]. A time-modulated Josephson-junction-based, triple-pumped reconfigurable circulator/directional amplifier—capable of high-performance non-reciprocal operation without magnetic fields—has been demonstrated for quantum information applications [19]. This approach leverages three-wave mixing to achieve dynamic switching between amplification and circulation modes, offering on-chip compatibility and low noise. Recently, time-modulation-based nonreciprocity has garnered significant attention due to its wide-ranging applications in modern wireless communication systems, photonics, radar technologies, and beyond [20, 21, 22, 23, 24, 25, 26, 27]. It exhibits dynamic properties characterized by the modulation of electrical permittivity, magnetic permeability, or electrical conductivity across both space and time [28, 29, 30, 31, 32]. Understanding their behavior is

crucial for designing advanced devices and systems with enhanced functionality and performance. Space-time metasurfaces are realized at microwave [33, 34, 35] and optical frequencies [36] for various functionalities, including nonreciprocal transmission [26, 37], target recognition [38], isolators [39, 40, 41], frequency conversion [42, 43], static-to-dynamic field conversion [44], parametric amplification [45], multiple access secure communication systems [46, 47], nonreciprocal antennas [48], coding metasurfaces [49], and multifunctional operations [20, 50]. However, traditional time-modulated devices and frequency converters and associated electronic components, such as varactors, transistors, and diodes, fall short in the millikelvin-temperature environments of superconducting quantum technologies due to their operational limitations and the noise they introduce.

Here, we present an experimental design of a quantum-compatible superconducting metasurface, operating at millikelvin temperatures, and incorporating cascaded space-time-modulated JoFETs. Josephson junctions, ubiquitous in superconducting electronics [51, 52], leverage the quantum mechanical phenomenon of supercurrent flow without resistance, offering unparalleled opportunities for nonlinear light manipulation [53, 54]. The proposed space-time-modulated metasurface mediates nonreciprocal coupling between frequency-distinct qubits, breaking Lorentz reciprocity via synthetic gauge fields imposed by the metasurface's spatiotemporal modulation. This approach differs fundamentally from JPA/JTWPA architectures, as it requires no external magnetic bias or circulators—key limitations of conventional nonreciprocal microwave devices. This study introduces a mechanism for nonreciprocal entanglement between two frequency-distinct qubits. Such a nonreciprocal entanglement presents new opportunities for quantum teleportation, memory storage, and scalable quantum networks, particularly in systems where qubits operate at different frequencies or energy states. Our nonlinear space-time-modulated metasurfaces, incorporating JoFETs [55, 56, 57], address these issues by providing highly efficient state-frequency conversion with superior performance in quantum applications. This approach enables miniaturization and integration of frequency converters while preserving quantum state integrity.

Our space-time-modulated metasurface offers critical capabilities beyond conventional 1D Josephson traveling-wave parametric amplifiers (JTWPAs): (a) Dimensionality—Homogeneous modulation in both z and y directions enables oblique photon transmission across 2D qubit arrays, overcoming the linear connectivity constraint of 1D systems. (b) Frequency agility—Arbitrary-frequency qubit pairs can be coupled, unlike JTWPAs that require fixed pump-dependent frequency relations. (c) Directional control—Momentum-selective coupling via 2D modulation achieves intrinsic nonreciprocity without external isolators. (d) Scalability—Parallel entanglement operations are facilitated by simultaneous multi-qubit coupling, avoiding the pump-phase crosstalk of 1D architectures. (e) Experimental simplicity—Nonreciprocity emerges from spatiotemporal modulation alone, eliminating the need for magnetic fields or complex pump schemes. (f) Versatility—The metasurface's synthetic gauge field supports reconfigurable entanglement protocols, a feature absent in static JTWPA designs. These advantages position our platform as a scalable solution for 2D quantum processors requiring high connectivity and frequency-multiplexed operations.

By harnessing the inherent nonlinearity of these JoFETs and orchestrating their spatial and temporal modulation, our work pioneers a new frontier in state-frequency conversion. Key features of our approach include efficient state-frequency conversion of incident photons, along with significant frequency conversion and amplification. In linear STM media, the wave equation produces coupled differential equations for each harmonic, with low modulation frequencies allowing strong coupling and efficient sideband generation [58, 59]. Nonlinear systems, however, introduce higher-order terms that enable efficient harmonic generation even at high modulation frequencies. Space-time-modulated superconducting metasurfaces, particularly with JoFETs, achieve high-efficiency state-frequency conversion at large modulation-to-signal frequency ratios. Unlike linear systems, which are constrained by phase-matching and dispersion and require long interaction lengths, nonlinear superconducting STM media deliver superior performance in a compact size, making them ideal for millikelvin temperature superconducting quantum technologies.

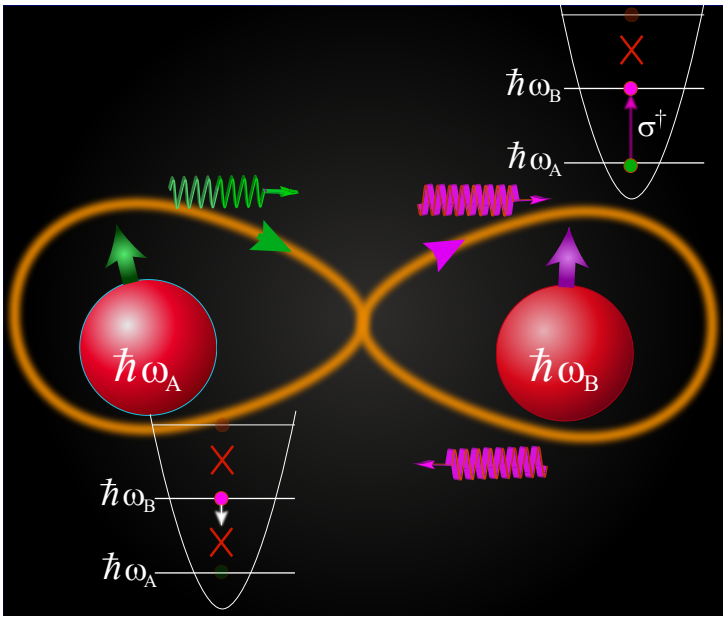

Figure 1: Nonreciprocal entanglement of frequency-distinct particles.

2 Nonreciprocal Entanglement of Frequency-Distinct Qubits

Figure 1 illustrates nonreciprocal entanglement of two frequency-distinct particles. In this scenario, a measurement on qubit A influences the state of qubit B, while a measurement on qubit B does not affect qubit A, thereby introducing directionality to the collapse of the entangled state. This departure from the symmetric nature of traditional entanglement is achieved by inducing a spatiotemporal asymmetry in the quantum interaction via a space-time-modulated superconducting metasurface. Applications include quantum state transfer in quantum computing and communication, where the quantum information from qubit A is transferred to qubit B (e.g., for quantum teleportation or memory) without reciprocal influence. This mechanism is also ideal for quantum networks, where information is transmitted between distant qubits operating at different frequencies. In this system, entanglement is initiated by qubit A, in the state $\hbar\omega_{\rm A}$, transferring its quantum information to qubit B, in the state $\hbar\omega_{\rm B}$, but the process does not reverse, as qubit B cannot influence qubit A. The directional frequency-conversion coupling provided by the space-time-modulated metasurface ensures that the entanglement process is asymmetric. The interaction allows qubit A to influence and entangle with qubit B, while qubit B remains unable to reciprocate. Once the entangled state is generated, the propagation of quantum information occurs in only one direction, facilitating one-way communication or information transfer in quantum technologies. For instance, a superconducting qubit operating at microwave frequencies could be entangled with a photonic qubit operating at optical frequencies. By converting and transferring quantum states between these different frequency domains, we enable entanglement across physically distinct qubit types. Here, the two qubits are in a superposition of joint states, as

$$|\psi\rangle = \alpha|0\rangle_{\rm A}|1\rangle_{\rm B} + \beta|1\rangle_{\rm A}|0\rangle_{\rm B} \tag{1}$$

where α and β are complex numbers. Here, qubits are in a correlated state across their different frequencies, even though each individual qubit has a distinct energy level (or frequency). Measurement of one qubit collapses the state of the other, proving they are entangled.
Figure 2 illustrates nonreciprocal entanglement of two frequency-distinct qubits via a spatiotemporal superconducting metasurface, featuring an array of cascaded space-time-modulated superconducting junctions. The metasurface offers a unique one-way state-frequency conversion from $\hbar\omega_{\rm A}$ to $\hbar\omega_{\rm B}$. The metasurface is characterized by a space-time-varying current density, expressed as $J(z,t) = I_0 \sin[\rho(z,t)]$, where I_0 is the critical current, and $\rho(z,t)$ represents the gauge-invariant phase difference across the Joseph-

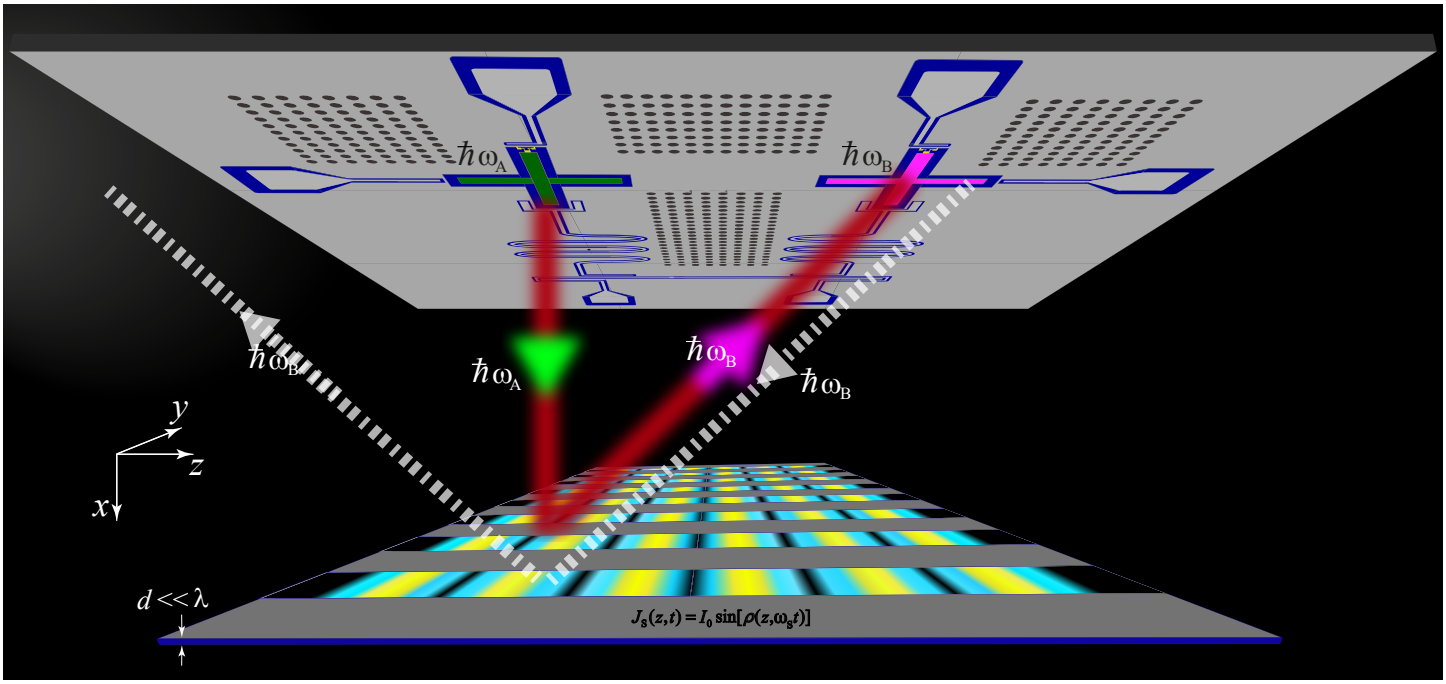

Figure 2: Nonreciprocal quantum state transfer of two frequency-distinct qubits via a spatiotemporal superconducting metasurface.

son junction, incorporating both spatial (z) and temporal (t) dependencies of the superconducting phase and electromagnetic vector potential. When a signal wave with frequency ω_0 is normally incident on the metasurface, and the modulation frequency is set to ω_s, a pure state-frequency conversion occurs, resulting in a new frequency $\omega_0 + \omega_s$. The converted signal exhibits conversion gain, demonstrating highly efficient state-frequency conversion with the desired high/low conversion frequency ratio, conversion gain, and spurious-free operation. This behavior is typical of the proposed metasurface, which can be further tailored to achieve other desired state-frequency conversion outcomes—such as down-conversion, low/high frequency conversion, or different conversion gains—through appropriate design of the space-time modulation's band structure and parameters. The proposed scheme facilitates this by providing a mechanism for cross-platform entanglement.

In quantum computing and communication, maintaining coherence and preventing noise are crucial for the proper functioning of qubit systems. One major challenge arises from back-action and frequency mismatch between qubits, which can interfere with their entanglement and disrupt quantum information transfer. By incorporating a nonreciprocal spatiotemporal superconducting metasurface, we can ensure unidirectional quantum state transfer and efficient frequency conversion between qubits at different energy levels. This section outlines how the metasurface addresses these challenges, enabling robust entanglement in quantum systems despite frequency detuning and eliminating unwanted interactions.

In practical quantum systems, different qubits often operate at different energy levels (or equivalently, different frequencies), to avoid cross-talk and interference. These differences in energy levels (often referred to as frequency detuning) make direct interaction between qubits at different frequencies difficult. Such a metasurface offers one-way state-frequency conversion, where a qubit operating at frequency ω_A can interact with another qubit operating at frequency ω_B. This conversion allows the two qubits to exchange quantum information and become entangled despite their energy-level differences. The ability to control the direction of state-frequency conversion ensures that the state transfer between the qubits is coherent and lossless, which is critical for establishing and maintaining entanglement.

3 Spatiotemporal Superconducting Metasurface

The space-time-varying inductance of the space-time-periodic superconducting metasurface reads

$$L_{\rm s}(I,z,t)=\frac{\Phi_0}{2\pi I_0}\sec\left(\widetilde{\Phi}_{\rm dc}+\widetilde{\Phi}_{\rm rf}\sin[\kappa_{\rm s}z-\omega_{\rm s}t+\phi]\right), \tag{2}$$

where $\kappa_{\rm s}$ is the spatial frequency of the modulation, $\widetilde{\Phi}_{\rm dc}=2\pi\Phi_{\rm dc}/\Phi_0$, $\widetilde{\Phi}_{\rm rf}=2\pi\Phi_{\rm rf}/\Phi_0$. Here, $\Phi_{\rm dc}$ and $\Phi_{\rm rf}$ are static and dynamic modulation amplitudes, and Φ_0 is the magnetic flux quantum. The corresponding time-varying permeability of the JoFET array reads

$$\mu_{\rm s}(I,z,t)=\frac{lL_{\rm s}(I,z,t)}{\mu_0 A}, \tag{3}$$

where l and A are the length and area of the Josephson junction, respectively. As the nonlinear permeability of JoFETs exhibits periodicity in both space and time, it can be represented by a Fourier series expansion, i.e.,

$$a(I,z,t)=\frac{1}{\mu_{\rm s}(I,z,t)}=\sum_{m=-\infty}^{+\infty}a_m e^{-jm(\kappa_{\rm s}z-\omega_{\rm s}t+\phi)}. \tag{4}$$

and then, determine the unknown coefficients in Eq.(4) using the Taylor series expansion.
We consider two superconducting qubits with transition frequencies ω_A and ω_B, coupled through a nonlinear Josephson metasurface whose inductance is modulated in both space and time. The full quantum Hamiltonian comprises three components, as

$$H=H_q+H_s+H_{int}, \tag{5a}$$

where the qubit Hamiltonian reads

$$H_q=\hbar\omega_A\sigma_a^+\sigma_a^-+\hbar\omega_B\sigma_b^+\sigma_b^-, \tag{5b}$$

the metasurface Hamiltonian (spatial harmonics) is given by

$$H_s=\sum_{m=-\infty}^{\infty}\hbar m\omega_s b_m^\dagger b_m, \tag{5c}$$

and the interaction Hamiltonian is represented by

$$H_{int}=\sum_m\hbar\left(g_{ab}^{(m)}\sigma_a^+\sigma_b^-b_m e^{i\phi}+g_{ba}^{(m)}\sigma_a^-\sigma_b^+b_m^\dagger e^{-i\phi}\right)+\text{H.c.}, \tag{5d}$$

where b_m ($b_m^\dagger$) annihilates (creates) a photon in the m-th metasurface mode with wavevector $m\kappa_s$ and frequency $m\omega_s$. The system's evolution is governed by a Lindblad master equation, as

$$\dot\rho=-\frac{i}{\hbar}[H,\rho]+\sum_m\gamma_m\left(b_m\rho b_m^\dagger-\frac{1}{2}\{b_m^\dagger b_m,\rho\}\right)+\mathcal{L}_q(\rho), \tag{5e}$$

where γ_m is the decay rate of metasurface mode m, and $\mathcal{L}_q$ models qubit decoherence (T_1 and T_2 processes). Under the conditions $\omega_s\gg g_{ab},g_{ba},\gamma_m$, we adiabatically eliminate the metasurface modes to obtain an effective non-Hermitian Hamiltonian for the qubits

$$H_{\rm eff}=H_q+\sum_m\left(\frac{\hbar|g_{ab}^{(m)}|^2}{\Delta_m+i\gamma_m/2}\sigma_a^+\sigma_b^-+\frac{\hbar|g_{ba}^{(m)}|^2}{\Delta_m-i\gamma_m/2}\sigma_a^-\sigma_b^+\right), \tag{5f}$$

where $\Delta_m=\omega_a-\omega_b-m\omega_s$. The imaginary terms ($\pm i\gamma_m/2$) break time-reversal symmetry, enabling nonreciprocity. For $g_{ba}\ll g_{ab}$ and initial state $|\psi(0)\rangle=(\alpha|0_a\rangle+\beta|1_a\rangle)\otimes|0_b\rangle$, the solution to first order in $g_{ab}t$ reads

$$|\psi(t)\rangle\approx(\alpha|0_a\rangle+\beta|1_a\rangle)\otimes\left(|0_b\rangle-it\beta\sum_m\frac{g_{ab}^{(m)}}{\Delta_m+i\gamma_m/2}|1_b\rangle\right), \tag{5g}$$

which demonstrates unidirectional state transfer from qubit a to b, with the transfer rate

$$\Gamma_{a\to b} = \left| \sum_m \frac{g_{ab}^{(m)}}{\Delta_m + i\gamma_m/2} \right|^2 . \tag{5h}$$

The concurrence $\mathcal{C}(t)$ quantifying entanglement grows as

$$\mathcal{C}(t) \approx 2|\alpha\beta|\Gamma_{a\to b}t, \tag{5i}$$

valid for $\Gamma_{a\to b}t \ll 1$. From the effective non-Hermitian Hamiltonian H_{eff}, we derive the equations of motion for the qubit density matrix elements $\rho_{ij} = \langle i|\rho_q|j\rangle$ $(i, j \in \{0_a0_b, 0_a1_b, 1_a0_b, 1_a1_b\})$

$$\dot{\rho}_{1_a0_b} = -i\left(\omega_a\rho_{1_a0_b} + \sum_m \frac{g_{ab}^{(m)}}{\Delta_m + i\gamma_m/2}\rho_{0_a1_b}\right) - \frac{\Gamma_{a\to b}}{2}\rho_{1_a0_b}, \tag{6a}$$

$$\dot{\rho}_{0_a1_b} = -i\left(\omega_b\rho_{0_a1_b} + \sum_m \frac{g_{ba}^{(m)}}{\Delta_m - i\gamma_m/2}\rho_{1_a0_b}\right) - \frac{\Gamma_{b\to a}}{2}\rho_{0_a1_b}. \tag{6b}$$

For $g_{ba} \ll g_{ab}$, these reduce to

$$\rho_{0_a1_b}(t) \approx -i\frac{g_{ab}}{\Delta + i\gamma/2}\rho_{1_a0_b}(0)\left(1 - e^{-i\Delta t - \Gamma_{a\to b}t/2}\right), \tag{6c}$$

showing asymmetric population transfer.

Given the periodicity of the metasurface in space and time, the magnetic field in the metasurface may be decomposed to Floquet space-time harmonics, as

$$\mathbf{H}_{\text{s}}(x, z, t) = \hat{\mathbf{y}} \sum_n \Psi_n e^{-j[k_x x + \kappa_n z - \omega_n t]}, \tag{7}$$

where k_x is the x-component of the wavenumber, given by $k_x = k_0\cos(\theta_{\text{i}})$, with $k_0 = \omega_0/c$ denoting the wavenumber of the incident light, and θ_{i} representing the angle of incidence between the incident wave and the metasurface boundary. Here, ω_0 is the angular frequency of the incident light, and c is the speed of light in vacuum. Furthermore, ω_n is the temporal frequency of the nth space-time harmonic, and $\kappa_n = \kappa_0 + n\kappa_{\text{s}}$ denotes the z-component of the wavenumber for the nth space-time harmonic inside the metasurface, with κ_0 being the z-component of the wavenumber for the fundamental space-time harmonic. Then, solving Maxwell's equations and truncating to $2N + 1$ terms gives the wave equation $[\mathbf{A}] \cdot [\overrightarrow{\Psi}] = 0$, where the matrix $[\mathbf{A}]$ reads

$$[\mathbf{A}] = \begin{bmatrix} v_{-N} & \tilde{\mu}_1 & \tilde{\mu}_2 & \cdots & \tilde{\mu}_{M-2} & \tilde{\mu}_{M-1} & \tilde{\mu}_M \\ \tilde{\mu}_{-1} & v_{-N+1} & \tilde{\mu}_1 & \cdots & \tilde{\mu}_{M-3} & \tilde{\mu}_{M-2} & \tilde{\mu}_{M-1} \\ \tilde{\mu}_{-2} & \tilde{\mu}_{-1} & v_{-N+2} & \cdots & \tilde{\mu}_{M-4} & \tilde{\mu}_{M-3} & \tilde{\mu}_{M-2} \\ \vdots & \vdots & \vdots & \ddots & \vdots & \vdots & \vdots \\ \tilde{\mu}_{-M+2} & \tilde{\mu}_{-M+3} & \tilde{\mu}_{-M+4} & \cdots & v_{N-2} & \tilde{\mu}_1 & \tilde{\mu}_2 \\ \tilde{\mu}_{-M+1} & \tilde{\mu}_{-M+2} & \tilde{\mu}_{-M+3} & \cdots & \tilde{\mu}_{-1} & v_{N-1} & \tilde{\mu}_1 \\ \tilde{\mu}_{-M} & \tilde{\mu}_{-M+1} & \tilde{\mu}_{-M+2} & \cdots & \tilde{\mu}_{-2} & \tilde{\mu}_{-1} & v_N \end{bmatrix}, \tag{8a}$$

where $\tilde{\mu}_m = 1/a_m$, and $v_n = \tilde{\mu}_0 - (k_x^2 + \kappa_n^2)/k_n^2$. In Eq. (8a), the integer M is the truncation order for the Fourier series harmonics of the space-time-varying permeability (Eq. (3)), ensuring Eq. (4) provides an accurate representation. Similarly, N is the truncation order for the number of space-time harmonics for the electromagnetic fields in Eq. (7). For weakly nonlinear Josephson inductance regimes, numerical convergence is achieved with $M = 4$ and $N = 5$, balancing computational efficiency and accuracy. For non-trivial solutions (i.e., $[\overrightarrow{\Psi}] \neq 0$), the matrix $[\mathbf{A}]$ must be singular, meaning its determinant is zero, that is,

$$\det[\mathbf{A}] = 0, \tag{8b}$$

The condition in Eq. (8b) ensures that the system supports light propagation and provides the dispersion relation, typically expressed as $\omega(k)$ or $k(\omega)$. The matrix $[\mathbf{A}]$ contains material parameters such as permittivity, permeability, and conductivity, all of which affect wave propagation. The elements of $[\mathbf{A}]$ depend on the wavevector (κ_n) and frequency (ω_n), establishing a connection between them. By setting $\det[\mathbf{A}] = 0$, we find the conditions under which the system supports light propagation. This relation describes how frequency and wavevector are related, i.e., $\omega_n(\kappa_n)$ or $\kappa_n(\omega_n)$, and provides information about allowed frequencies, wavevectors, group velocity, phase velocity, and band structures. In essence, Eq. (8b) serves as a condition for photon transmission, and solving this equation reveals the dispersion relation, which characterizes wave behavior in the system.

The matrix $[\mathbf{A}]$, along with the truncated a_n coefficients (noting that, theoretically, an infinite number of elements exist), demonstrates the impact of nonlinearity. In nonlinear systems, energy from the primary harmonic modes (A_{nn}) is distributed across an infinite series of adjacent harmonic modes (A_{nm}, where $n \neq m$, $-\infty < n, m < +\infty$). This differs from linear space-time-modulated media [59], where energy from the main harmonic modes (A_{nn}) is distributed only to the immediately adjacent harmonic modes ($A_{n,n-1}$ and $A_{n,n+1}$). Nonlinear systems, however, enable redistribution of energy across a broader spectrum of harmonic frequencies, allowing efficient energy transfer from the incident wave to higher-frequency harmonic modes. This is because nonlinear interactions can sustain the high-frequency modulation necessary for such transfers. Considering the incident field $\mathbf{H}_{\mathrm{I}}(x,z,t) = \hat{\mathbf{y}} H_0 e^{j\omega_0 t} \cdot e^{-j[k_0 \sin(\theta_{\mathrm{i}})x + k_0 \cos(\theta_{\mathrm{i}})z]}$, the reflected fields reads

$$\mathbf{H}_{\mathrm{R}}(x,z,t) = \hat{\mathbf{y}} \sum_{n=-\infty}^{\infty} R_n e^{-j\left[k_0 \sin(\theta_{\mathrm{i}})x - k_{0n} \cos(\theta_n^{\mathrm{R}})z - \omega_n t\right]}, \tag{9}$$

where θ_n^{R} is defined as the angle between the nth reflected space-time harmonic and the metasurface boundary. We apply continuity of the tangential components of the electromagnetic fields at $z = 0$ and $z = d$ to find the unknown field amplitudes R_n.

4 Results

Figure 3 illustrates a schematic of the experimental prototype design of the space-time-modulated Josephson metasurface. The proposed spatiotemporal JoFET unit cell utilizes an Al-proximitized InAs quantum well, grown on a semi-insulating Fe counter-doped (100) InP wafer, providing a voltage-controlled Josephson junction. The proposed spatiotemporal Josephson Field-Effect Transistor (JoFET) unit cell utilizes an Al-proximitized InAs quantum well, grown on a semi-insulating Fe counter-doped (100) InP wafer. Device patterning would be performed using a high-precision electron-beam lithography system, such as the Raith EBPG 5100. To form the Josephson weak link, a trench could be etched into the aluminum layer using a commercial etchant like Transene D at 50°C for approximately 5 seconds. The trench is designed to be around 20 nm in length and 25 μm in width, though some variance, such as a width of about 50 nm, may be observed upon inspection using scanning electron microscopy (SEM). The superconductor-semiconductor mesa, serving as the center pin of the coplanar waveguide (CPW) resonator, would be created by masking with polymethyl methacrylate (PMMA) followed by a semiconductor wet etch using a CH_3COOH-H_2O_2-H_3PO_4 mixture for roughly 150 seconds at room temperature. For the ground plane, the scenario involves the evaporation of a 5 nm titanium (Ti) layer followed by a 50 nm niobium (Nb) layer. Prior to deposition, a brief 1-minute argon ion milling at 400 V, with an ion current of 21 mA, could be conducted in an ultrahigh-vacuum (UHV) evaporator, such as a Plassys system, to ensure a clean metasurface. The dielectric layer between the gate and the junction would be deposited via an atomic layer deposition (ALD) process, using a thermal ALD alumina procedure at 150°C for about 150 cycles, resulting in an approximate thickness of 12 nm. The gate, which covers the Josephson weak link area, would then be formed by evaporating an 8 nm titanium (Ti) layer followed by an 80 nm gold (Au) layer, deposited at a 30° tilt with 5-rpm planetary rotation in a high-vacuum (HV) evaporator, such as the Plassys. For all lift-off and cleaning procedures, hot acetone at 50°C followed by isopropanol rinsing would be recommended.

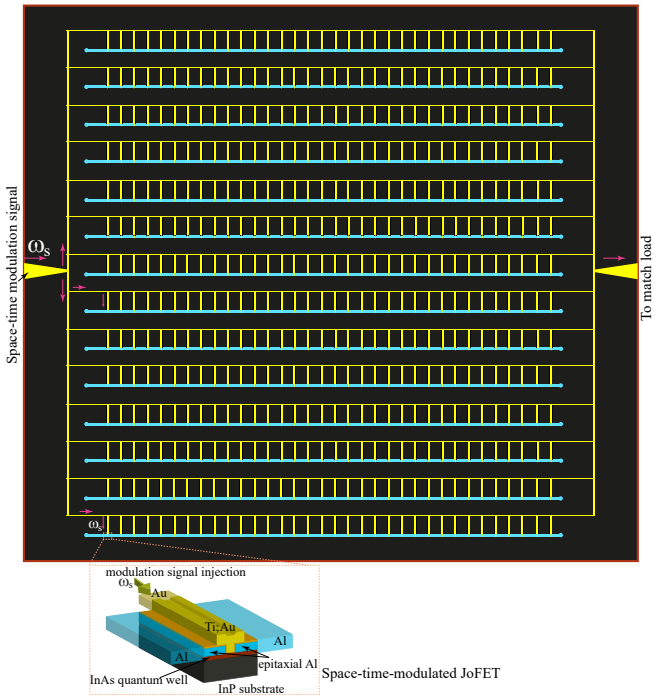

Figure 3: Schematic of the experimental prototype design of the space-time-modulated Josephson metasurface.

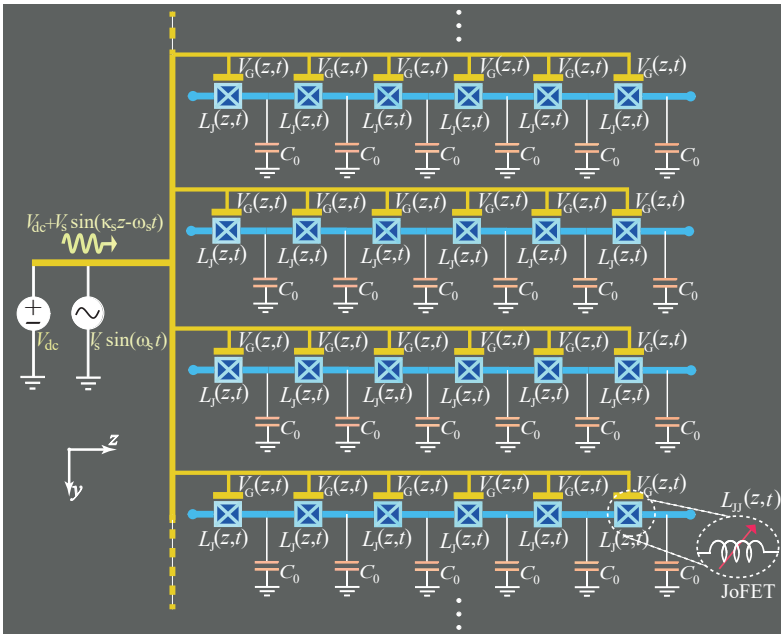

Figure 4: Equivalent circuit of the designed spatiotemporal metasurface composing a 2D array of gated superconductor-semiconductor JoFETs.

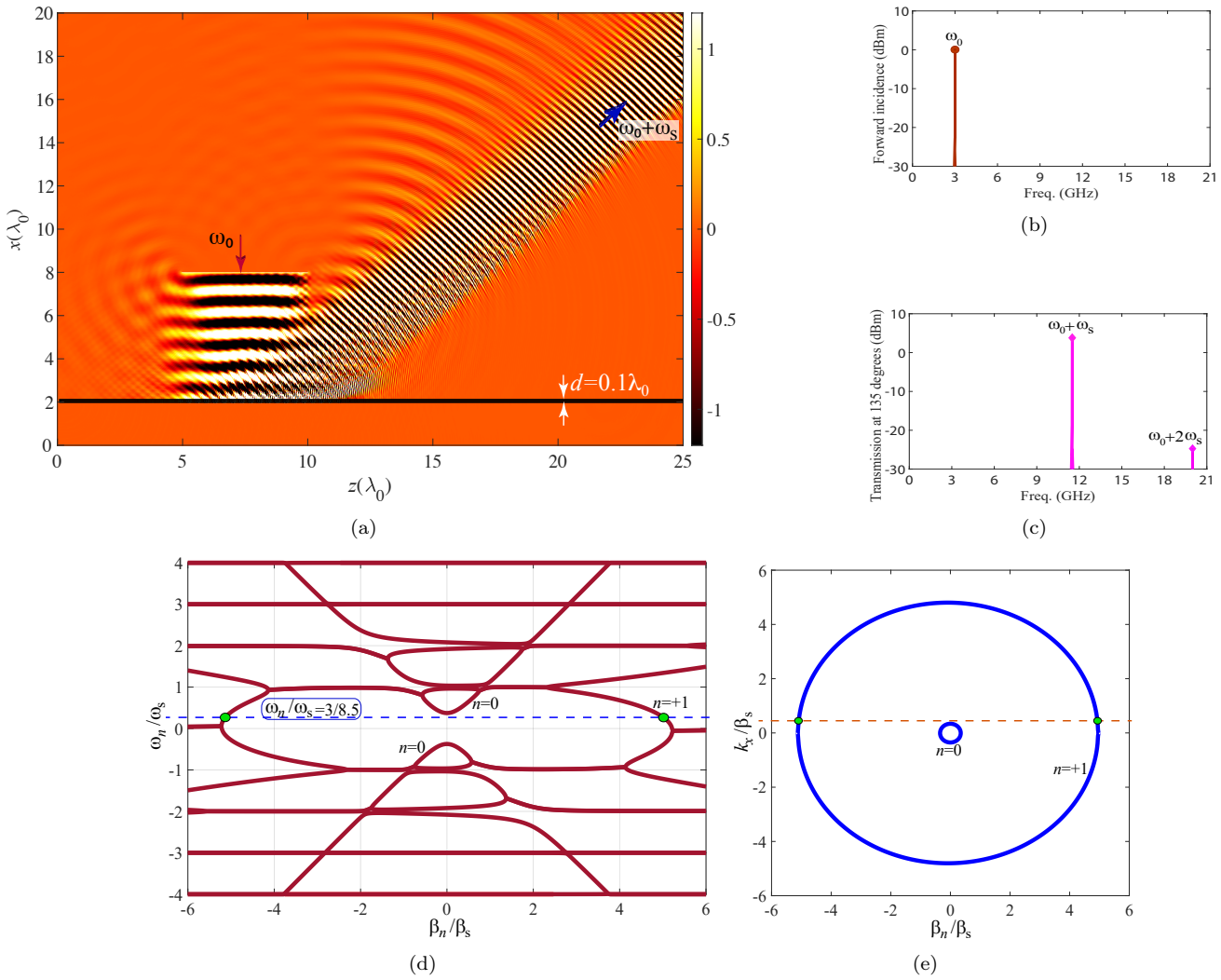

Figure 5: Pure quantum state-frequency conversion by a space-time-modulated superconducting metasurface. (a) FDTD numerical simulation results for magnetic field distribution H_y. Normal excitation results in a highly efficient state-frequency conversion from $\omega_0 = 2\pi \times 3$ GHz to $\omega_0 + \omega_s = 2\pi \times 11.5$ GHz. (b) and (c) Frequency spectrum of the incident photon and the *up-converted* reflected photon at $\theta_r = 135°$, respectively. (d) Band structure, showing excitation of the first higher state ($n = +1$) at $\omega_0/\omega_s = 3/8.5$. (e) Isofrequency dispersion diagram.

Figure 4 illustrates the equivalent circuit model of the proposed spatiotemporal metasurface enabling nonreciprocal entanglement between distinct-frequency qubits. The metasurface is featuring a 2D array of JoFETS. Space-time modulation is achieved through a periodic signal traveling along the yellow lines and spatiotemporally modulate the gate voltage of JoFETs. To demonstrate the capability of the proposed apparatus in nonreciprocal pure state-frequency conversion, we design a metasurface with the thickness $d = 0.1\lambda$, and the space-time-varying permeability given by $\mu_s(z,t) = \sec(0.75 + 0.78\sin[2\pi \times 8.5 \times 10^9(z/c - t)])$. Figure 5(a) presents the simulation results for forward light excitation, where a wave at $\omega_0 = 2\pi \times 3$ GHz is directed at an angle of $\theta = 0°$. The incident light is reflected by the metasurface, which has a thickness of $d = 0.1\lambda$, undergoing a pure frequency up-conversion from $\omega_0 = 2\pi \times 3$ GHz to $\omega_0 + \omega_s = 2\pi \times 11.5$ GHz.

Figure 5(a) presents the FDTD numerical results for the magnetic field distribution H_y, illustrating the state-frequency conversion capability of the proposed JoFET-based spatiotemporal metasurface. The metasurface, composed of a semiconductor-superconductor heterostructure, is excited normally, resulting in a highly efficient frequency conversion from the initial state at $\omega_0 = 2\pi \times 3$ GHz to a higher state at $\omega_0 + \omega_s = 2\pi \times 11.5$ GHz. This process demonstrates the effective manipulation of quantum states associated with different frequency domains. A notable conversion gain of 4.46 dB is achieved, under-

scoring the high efficiency of the proposed metasurface. The state-frequency conversion ratio of 3.83 further demonstrates the system's potential for practical quantum applications, particularly in mediating entanglement between two frequency-distinct qubits. This capability highlights the metasurface's role in enabling efficient quantum state transfer across different energy levels, a critical feature for advancing quantum communication and computing technologies. Figures 5(b) and 5(c) plot the the frequency spectrum of the incident photon and the transmitted up-converted photon at $\omega_0 + \omega_s = 2\pi \times 11.5$ GHz under a reflection angle of $\theta_r = 135°$, as shown in Fig. 5(a). The observed spectral purity in the converted photon highlights the metasurface's remarkable ability to achieve a pristine state-frequency conversion process, devoid of unwanted mixing products or spurious signals. This feature underscores the efficacy of the proposed metasurface design in enabling high-fidelity state-frequency conversion, crucial for various applications in communication systems, quantum computing, and beyond.

To gain deeper insight into this phenomenon, we analyse the band structure and isofrequency diagram of the system, as plotted using Eq.(8b), shown in Figs. 5(d) and 5(e), respectively. The band structure in Fig. 5(d) reveals excitation of the first higher state space-time mode ($n = +1$) at the excitation frequency $\omega_0/\omega_m = 3/8.5$, where the fundamental space-time mode is not excited. The isofrequency dispersion diagram in Fig. 5(e) confirms excitation of the first higher state space-time mode ($n = +1$) at the given incidence angle of $\theta_i = 90°$, where $k_x/\beta_s = 3\sin(\theta_i)/8.5 = 0.352\sin(\theta_i)$.

To demonstrate the nonreciprocal response of the metasurface, we examine the backward excitation scenario, where a photon similar to the output (reflected up-converted photon) of the forward excitation is incident upon the metasurface. Specifically, a photon at $\omega_0 + \omega_s = 2\pi \times 11.5$ GHz is directed at an angle of $\theta = 135°$. Figure 6(a) illustrates the time-domain results, indicating that the photon approaching from the right is reflected to the left by the metasurface without undergoing state-frequency conversion. In contrast, a reciprocal metasurface would exhibit reflection at 0° with a down-converted frequency of $2\pi \times 3$ GHz, corresponding to the initial excitation state of the forward incidence.

Figure 6(b) plots the frequency spectrum of the incident photon at $\omega_0 + \omega_s = 2\pi \times 11.5$ GHz under an incidence angle of $\theta_i = 135°$, as shown in Fig. 5(a). Figure 6(c) plots the frequency spectrum of the reflected photon under an incidence angle of $\theta_i = 45°$, as shown in Fig. 5(a). Figure 6(c) shows that a pure specular reflection with no state-frequency conversion is provided by the metasurface, which is in contrast to the forward case, where excitation of the metasurface under normal incidence yields state-frequency up-conversion under a reflection angle of 135°. Such functionality offers an ideal platform for nonreciprocal entanglement between distinct-frequency superconducting qubits, as depicted in Fig. 2.

The band structure and isofrequency diagram of the backward excitation are plotted using Eq.(8b), shown in Figs. 6(d) and 6(e), respectively. The band structure in Fig. 6(d) reveals excitation of the fundamental state space-time mode ($n = 0$) at the excitation frequency $\omega_0/\omega_m = 11.5/8.5$. The isofrequency dispersion diagram in Fig. 6(e) confirms excitation of the fundamental state space-time mode ($n = 0$) at the given incidence angle of $\theta_i = 135°$, where $k_x/\beta_s = 11.5\sin(\theta_i)/8.5 = 1.353\sin(\theta_i)$.

5 Discussion

5.1 Nonlinear versus Linear STM Media

In linear space-time-modulated (STM) media, sideband generation is typically efficient only when the modulation frequency is much smaller than the carrier frequency ($\omega_m \ll \omega_0$). This limitation arises due to three key factors as follows.

- Dispersion effects: As ω_m increases, dispersion causes wavevector mismatches between the incident wave and the generated sidebands, degrading phase-matching conditions and reducing conversion efficiency.

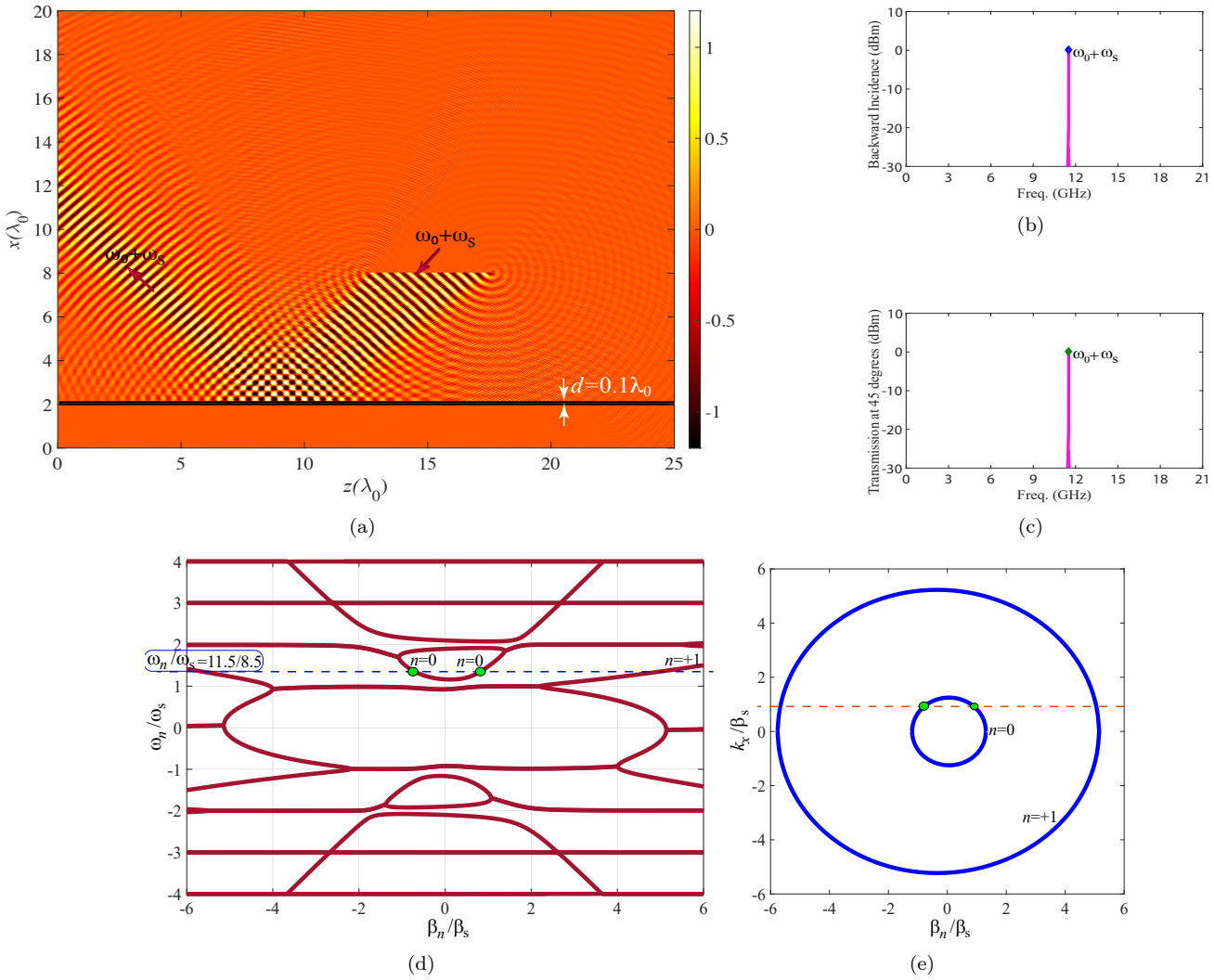

Figure 6: Nonreciprocity test: (a) Time domain response for oblique excitation (at 135°) of the proposed metasurface, shown in Fig. 5(a), at $\omega_0+\omega_s = 2\pi\times 11.5$ GHz results in no quantum state-frequency conversion, but instead reflects the incident photon to the left at the same frequency. (b) Frequency spectrum of the incident photon. (c) Frequency spectrum of the reflected photon at $\theta_r = 45°$. (d) Band structure, showing excitation of the ground state ($n = 0$) at $\omega_0/\omega_s = 11.5/8.5$. (e) Isofrequency dispersion diagram, demonstrating excitation of the ground state ($n = 0$).

- Phase-matching constraints: When $\omega_{\mathrm{m}} \ll \omega_0$, the modulation's spatiotemporal periodicity aligns well with the incident wavelength, maximizing energy transfer to sidebands ($\omega_0 \pm n\omega_{\mathrm{m}}$). At higher ω_{m}, this alignment deteriorates.
- Interaction length: Low-frequency modulations preserve a longer effective interaction length, allowing sustained energy coupling. For $\omega_{\mathrm{m}} \sim \omega_0$, the interaction length shortens, curtailing sideband growth.

Consequently, linear STM media are poorly suited for applications requiring high-ratio or large-signal state-frequency conversion, where strong sidebands at $\omega_{\mathrm{m}} \gtrsim \omega_0$ are essential. Beyond inefficiency at higher modulation frequencies, linear STM systems suffer from in-band space-time harmonics—unwanted spectral components generated within the operational bandwidth due to the periodic modulation of material parameters (e.g., $\epsilon(z,t) = \epsilon_{\mathrm{r}} + \delta\cos(\omega_{\mathrm{m}}t - \beta_{\mathrm{m}}z)$). These harmonics introduce several practical challenges:

- Intermodulation distortion (IMD): Mixing of multiple harmonics with the carrier or sidebands creates spurious frequencies (e.g., $2\omega_0 \pm \omega_{\mathrm{m}}$, $\omega_0 \pm 2\omega_{\mathrm{m}}$), degrading signal integrity in communication or sensing systems.
- Spectral crowding: Dense harmonic generation complicates filtering and increases noise, especially in multi-tone or broadband applications.
- Power loss: Energy diverted to parasitic harmonics reduces the power available for target sidebands, further limiting conversion efficiency.

Critically, these issues stem from the passive, weak-coupling nature of linear STM systems, where modulation acts as a perturbation rather than a controlled nonlinear interaction. .
In contrast to linear spatiotemporal media, superconducting nonlinear STM metasurfaces (e.g., Josephson-junction-based systems) enable efficient high-ratio state-frequency conversion, even for $\omega_{\mathrm{s}} > \omega_0$. This capability stems from their intrinsic nonlinear dynamics, which overcome the fundamental limitations of linear systems through the following mechanisms:

- Nonlinear Harmonic Generation and Broadband Mixing: Unlike linear media, where harmonic generation is weak and limited to low orders, nonlinear STM systems produce higher-order harmonics ($\omega_0 \pm n\omega_{\mathrm{s}}$) with significant power. The nonlinear response (e.g., current-phase relations in Josephson junctions) ensures that energy couples not only to the first few sidebands but across a broad spectrum, even at high modulation frequencies. This is because nonlinear terms (e.g., $\propto \phi^3$ in junction potentials) scale with amplitude, making their contribution dominant as ω_{s} increases.
- Phase-Matching Relaxation and Active Dispersion Compensation: Linear STM media rely critically on phase matching, which fails at $\omega_{\mathrm{s}} \sim \omega_0$ due to dispersion. Nonlinear systems circumvent this via:

  - Self-tuning wavevector alignment: Nonlinearities (e.g., parametric coupling in JoFETs) dynamically adjust the effective refractive index, compensating for dispersion and maintaining efficient energy transfer.

  - Amplitude-dependent phase shifts: The wave interaction itself modifies the local propagation conditions, reducing sensitivity to strict phase-matching constraints.
- Controlled Energy Redistribution: Nonlinear STM media actively redistribute energy across harmonics through processes like four-wave mixing or parametric amplification. When $\omega_{\mathrm{s}} > \omega_0$, energy from the pump ($\omega_0$) is efficiently channeled to sidebands because:

  - The nonlinear interaction preserves momentum while accommodating high-frequency modulation.

  - Power-dependent effects (e.g., saturation) stabilize the energy distribution, preventing depletion of the fundamental mode.

- Modulation-Induced Nonlinear Instabilities: At high modulation frequencies ($\omega_s \gtrsim \omega_0$), nonlinear systems exhibit instabilities (e.g., parametric or modulation instability) that enhance sideband generation. These arise from:

  - Exponential gain regimes: Certain sidebands experience growth rates exceeding linear loss mechanisms.

  - Bifurcation phenomena: Threshold-driven transitions (e.g., in Josephson systems) abruptly amplify target frequencies.

- Suppression of Parasitic Effects: While linear STM media suffer from intermodulation distortion and uncontrolled harmonics, nonlinear systems can filter spurious content through:

  - Selective harmonic suppression: Nonlinear resonances (e.g., Josephson plasma oscillations) naturally attenuate undesired frequencies.

  - Directional coupling: Nonreciprocal frequency conversion (e.g., in gyrotropic metasurfaces) isolates target sidebands.

The ability of nonlinear spatiotemporal superconducting media to efficiently convert frequencies at high modulation-to-signal frequency ratios ($\omega_s > \omega_0$) is particularly useful superconducting quantum technologies at miliKelvin temperatures. These systems often require precise control over state-frequency conversion processes, and the nonlinear behavior allows for more flexible and efficient design of frequency converters, mixers, and modulators that can operate at higher frequencies without the limitations imposed by linear systems.

5.2 STM Superconducting Metasurface vs. Conventional JPAs/JTWPAs

- Dimensionality and Wave Interaction: JPAs/JTWPAs are 1D transmission-line structures designed for collinear signal injection, where waves propagate along a single axis (e.g., coplanar waveguides). Their operation is inherently limited to on-axis interactions, with no capacity to control oblique wavefronts. However, our STM Metasurface: As a 2D array of subwavelength unit cells, the metasurface behaves as a homogeneous medium for oblique incidence, enabling angle-selective wave engineering. This allows
  a) Nonreciprocal beam steering: The spatiotemporal modulation (STM) phase ($\beta_s z$) couples momentum components, permitting frequency conversion for off-axis waves (e.g., Fig. 2, oblique pump).
  b) Spatial multiplexing: Multiple qubits can be entangled via independent angular channels, a feature impossible in 1D JTWPAs.

- Subwavelength Design and Homogeneity: The metasurface's subwavelength unit-cell spacing ensures incident waves (from any angle) interact with an effective homogeneous medium, unlike discrete JTWPA stages. This homogenization
  a) Suppresses diffraction effects that would arise in sparse arrays.
  b) Preserves phase coherence across the metasurface, critical for entanglement generation.

- Functional Advantages Over 1D Systems:
  a) Oblique Phase Matching: STM compensates for momentum mismatch via nonlinear dispersion tuning, whereas JTWPAs require strict alignment.
  b) Multi-angle nonreciprocity: A single metasurface can simultaneously support direction-dependent frequency conversion, enabling complex quantum routing.

- JPAs/JTWPAs: Fixed Pump Frequency Rules: In standard degenerate JPAs/JTWPAs, the pump frequency (ω_p) is typically set at twice the signal frequency ($\omega_p = 2\omega_s$) to enable phase-sensitive amplification (e.g., squeezing). This condition arises because
  a) The nonlinear inductance is pumped at $2\omega_s$ to parametrically couple signal (ω_s) and idler ($\omega_i = \omega_p - \omega_s = \omega_s$) modes, enabling gain.

b) This is a degenerate process where $\omega_s = \omega_i$ (energy conservation: $\omega_p = \omega_s + \omega_i$). However, in non-degenerate JPAs/JTWPAs, the pump frequency can differ. For example $\omega_p = \omega_s + \omega_i$ (e.g., $\omega_p \neq 2\omega_s$ if $\omega_s \neq \omega_i$), enabling frequency conversion between distinct signal/idler tones. This is used in quantum state transfer or frequency-mixing applications [17].

- Our STM Metasurface: Flexible Modulation Frequency In contrast, our spatiotemporally modulated (STM) metasurface imposes no fixed ratio between the modulation frequency (ω_s) and input frequencies (ω_1, ω_2). Key differences:
  a) Arbitrary ω_s: The modulation frequency ω_s is independent of qubit transition frequencies (ω_{q1}, ω_{q2}). It can be tuned to bridge any frequency gap (e.g., $\omega_s = |\omega_{q1} - \omega_{q2}|$) to mediate entanglement.
  b) Multi-frequency mixing: STM generates sidebands at $\omega_{q1} \pm n\omega_s$ and $\omega_{q2} \pm m\omega_s$, enabling nonreciprocal coupling even when $\omega_s \ll \omega_{q1}, \omega_{q2}$ (unlike JPA's $\omega_p \sim \omega_s$ constraint).
  c) Spatiotemporal phase matching: The metasurface's spatial modulation ($\beta_s z$) allows momentum conservation without requiring $\omega_p = 2\omega_s$ or $\omega_p = \omega_s + \omega_i$.
- Why This Distinction Matters?
  a) Flexibility: Our system does not require ω_s to match a harmonic of qubit frequencies, enabling broader compatibility with heterogeneous quantum devices.
  b) Nonreciprocity: The STM's traveling-wave modulation ($e^{i(\omega_s t - \beta_s z)}$) breaks Lorentz reciprocity, while JPAs/JTWPAs are typically reciprocal unless engineered otherwise (e.g., with circulators).
  c) Scalability: Simultaneous modulation at multiple ω_s can entangle multiple qubit pairs across different frequencies, a challenge for single-pump JTWPAs.

6 Conclusions

We demonstrated the potential of spatiotemporal superconducting metasurfaces for enabling nonreciprocal entanglement and quantum state transfer between frequency-distinct superconducting qubits. By leveraging cascaded space-time-modulated Josephson field-effect transistors (JoFETs), these metasurfaces overcome the limitations of traditional linear space-time media, offering efficient state-frequency conversion at millikelvin temperatures. The spurious-free quantum state conversion, coupled with the inherent unidirectionality of the space-time modulation, provides a promising avenue for advancing quantum technologies by enhancing coherence and reducing back-action. This novel platform lays the foundation for new quantum wave engineering approaches, particularly in systems where qubits with high frequency distinctions are involved.

References

[1] A. Einstein, B. Podolsky, N. Rosen, *Phys. Rev.* **1935**, *47*, 10 777.

[2] R. Horodecki, P. Horodecki, M. Horodecki, K. Horodecki, *Rev. Mod. Phys.* **2009**, *81*, 2 865.

[3] T. D. Ladd, F. Jelezko, R. Laflamme, Y. Nakamura, C. Monroe, J. L. O'Brien, *nature* **2010**, *464*, 7285 45.

[4] M. Erhard, M. Krenn, A. Zeilinger, *Nature Reviews Physics* **2020**, *2*, 7 365.

[5] M. Bock, P. Eich, S. Kucera, M. Kreis, A. Lenhard, C. Becher, J. Eschner, *Nat. Commun.* **2018**, *9*, 1 1998.

[6] B. Albrecht, P. Farrera, X. Fernandez-Gonzalvo, M. Cristiani, H. De Riedmatten, *Nat. Commun.* **2014**, *5*, 1 3376.

[7] N. Maring, D. Lago-Rivera, A. Lenhard, G. Heinze, H. de Riedmatten, *Optica* **2018**, *5*, 5 507.

[8] X. Han, W. Fu, C.-L. Zou, L. Jiang, H. X. Tang, *Optica* **2021**, *8*, 8 1050.

[9] T. Santiago-Cruz, S. D. Gennaro, O. Mitrofanov, S. Addamane, J. Reno, I. Brener, M. V. Chekhova, *Science* **2022**, *377*, 6609 991.

[10] J. F. Geus, F. Elsen, S. Nyga, A. J. Stolk, K. L. van der Enden, E. J. van Zwet, C. Haefner, R. Hanson, B. Jungbluth, *Optica Quantum* **2024**, *2*, 3 189.

[11] J. M. Gambetta, J. M. Chow, M. Steffen, *npj quantum information* **2017**, *3*, 1 2.

[12] Y. He, J. Liu, C. Zhao, R. Huang, G. Dai, W. Chen, *Journal of Superconductivity and Novel Magnetism* **2022**, *35*, 1 11.

[13] A. Berlin, R. T. D'Agnolo, S. A. Ellis, C. Nantista, J. Neilson, P. Schuster, S. Tantawi, N. Toro, K. Zhou, *Journal of High Energy Physics* **2020**, *2020*, 7 1.

[14] A. V. Dixit, S. Chakram, K. He, A. Agrawal, R. K. Naik, D. I. Schuster, A. Chou, *Phys. Rev. Lett.* **2021**, *126*, 14 141302.

[15] S. D. Bass, M. Doser, *Nat. Rev. Phys.* **2024**, 1–11.

[16] M. Castellanos-Beltran, K. Lehnert, *Applied Physics Letters* **2007**, *91*, 8.

[17] C. Macklin, K. O'brien, D. Hover, M. Schwartz, V. Bolkhovsky, X. Zhang, W. Oliver, I. Siddiqi, *Science* **2015**, *350*, 6258 307.

[18] J. Aumentado, *IEEE Microwave magazine* **2020**, *21*, 8 45.

[19] K. Sliwa, M. Hatridge, A. Narla, S. Shankar, L. Frunzio, R. Schoelkopf, M. Devoret **2015**, *5*, 4 041020.

[20] S. Taravati, C. Caloz, *IEEE Trans. Antennas Propagat.* **2017**, *65*, 2 442 .

[21] S. Taravati, A. A. Kishk, *Phys. Rev. B* **2019**, *99*, 7 075101.

[22] S. Taravati, A. A. Kishk, *IEEE Microw. Mag.* **2020**, *21*, 4 30.

[23] J. Wang, D. Feng, Y. Kong, S. Quan, S. Xing, *IEEE Transactions on Antennas and Propagation* **2022**, *70*, 7 5884.

[24] M. Saikia, K. V. Srivastava, *IEEE Transactions on Antennas and Propagation* **2022**, *71*, 2 1506.

[25] S. Taravati, A. A. Kishk, *IEEE Trans. Antennas Propagat.* **2019**, *67*, 1 270.

[26] S. Taravati, G. V. Eleftheriades, *Phys. Rev. Appl.* **2020**, *14*, 1 014027.

[27] D. M. Solís, N. Engheta, *Phys. Rev. B* **2021**, *103*, 14 144303.

[28] S. Wan, L. Cao, Y. Zhu, M. Oudich, B. Assouar, *Phys. Rev. Appl.* **2021**, *16*, 6 064061.

[29] S. Taravati, G. V. Eleftheriades, *IEEE Antennas Propag. Mag.* **2023**, *65*, 4 61.

[30] C. Amra, A. Passian, P. Tchamitchian, M. Ettorre, A. Alwakil, J. A. Zapien, P. Rouquette, Y. Abautret, M. Zerrad, *Phys. Rev. Res.* **2024**, *6*, 1 013002.

[31] S. Taravati, G. V. Eleftheriades, *Nat. Commun.* **2021**, *14* 4414.

[32] M. Valizadeh, L. Yousefi, M. Miri, *Sci. Rep.* **2024**, *14*, 1 7332.

[33] M. Saikia, K. V. Srivastava, S. A. Ramakrishna, *IEEE Trans. Antennas Propagat.* **2019**, *68*, 4 2937.

[34] S. Taravati, G. V. Eleftheriades, *ACS Photonics* **2022**, *9*, 2 305.

[35] A. Kumar, S. Kongari, Y. Chandrakapure, D. Sarkar, *Sci. Rep.* **2024**, *14*, 1 13874.

[36] J. Sisler, P. Thureja, M. Y. Grajower, R. Sokhoyan, I. Huang, H. A. Atwater, *Nat. Nanotechnol* **2024**, 1–8.

[37] A. E. Cardin, S. R. Silva, S. R. Vardeny, W. J. Padilla, A. Saxena, A. J. Taylor, W. J. Kort-Kamp, H.-T. Chen, D. A. Dalvit, A. K. Azad, *Nat. Commun.* **2020**, *11*, 1 1469.

[38] X. Wang, M. S. Tong, L. Zhao, *IEEE Trans. Microw. Theory Techn.* **2023**, *71*, 8 3446.

[39] H. Lira, Z. Yu, S. Fan, M. Lipson, *Phys. Rev. Lett.* **2012**, *109*, 3 033901.

[40] S. Taravati, *Phys. Rev. B* **2017**, *96*, 23 235150.

[41] S. Taravati, G. V. Eleftheriades, *Adv. Mater. Technol* **2021**, 2100674.

[42] S. Taravati, G. V. Eleftheriades, *Phys. Rev. Appl.* **2021**, *15*, 6 064011.

[43] S. Taravati, *Phys. Rev. B* **2018**, *97*, 11 115131.

[44] M. J. Mencagli, D. L. Sounas, M. Fink, N. Engheta, *Phys. Rev. B* **2022**, *105*, 14 144301.

[45] X. Zhu, J. Li, C. Shen, G. Zhang, S. A. Cummer, L. Li, *Phys. Rev. B* **2020**, *102*, 2 024309.

[46] S. Taravati, G. V. Eleftheriades, *Phys. Rev. Appl.* **2019**, *12*, 2 024026.

[47] H. B. Sedeh, M. M. Salary, H. Mosallaei, *IEEE Trans. Antennas Propagat.* **2021**, *70*, 1 664.

[48] J. Zang, A. Alvarez-Melcon, J. Gómez-Diaz, *Phys. Rev. Appl.* **2019**, *12*, 5 054008.

[49] L. Zhang, Z. X. Wang, R. W. Shao, J. L. Shen, X. Q. Chen, X. Wan, Q. Cheng, T. J. Cui, *IEEE Trans. Antennas Propagat.* **2019**, *68*, 4 2984.

[50] S. Taravati, G. V. Eleftheriades, *Phys. Rev. Appl.* **2020**, *14*, 5 054017.

[51] Y. Makhlin, G. Schön, A. Shnirman, *Rev. Mod. Phys.* **2001**, *73*, 2 357.

[52] R. Kleiner, X. Zhou, E. Dorsch, X. Zhang, D. Koelle, D. Jin, *Nat. Commun.* **2021**, *12*, 1 6038.

[53] M. Trepanier, D. Zhang, O. Mukhanov, S. M. Anlage, *Physical Review X* **2013**, *3*, 4 041029.

[54] E. Zack, D. Zhang, M. Trepanier, J. Cai, T. Tai, N. Lazarides, J. Hizanidis, S. M. Anlage, *Physical Review E* **2022**, *105*, 4 044202.

[55] W. Mayer, M. C. Dartiailh, J. Yuan, K. S. Wickramasinghe, E. Rossi, J. Shabani, *Nat. Commun.* **2020**, *11*, 1 212.

[56] J. O'Connell Yuan, K. S. Wickramasinghe, W. M. Strickland, M. C. Dartiailh, K. Sardashti, M. Hatefipour, J. Shabani, *Journal of Vacuum Science & Technology A* **2021**, *39*, 3.

[57] D. Phan, P. Falthansl-Scheinecker, U. Mishra, W. Strickland, D. Langone, J. Shabani, A. P. Higginbotham, *Phys. Rev. Appl.* **2023**, *19*, 6 064032.

[58] S. Taravati, N. Chamanara, C. Caloz, *Phys. Rev. B* **2017**, *96*, 16 165144.

[59] S. Taravati, *Phys. Rev. Appl.* **2018**, *9*, 6 064012.